

# Classification of particle shapes from lidar depolarization ratio in convective ice clouds compared to in situ observations during CRYSTAL-FACE

Vincent Noel,<sup>1</sup> David M. Winker,<sup>2</sup> Matthew McGill,<sup>3</sup> and Paul Lawson<sup>4</sup>

Received 8 April 2004; revised 18 August 2004; accepted 25 October 2004; published 29 December 2004.

[1] A technique to classify ice particles into different shape categories, based on lidar depolarization ratio, is considered. This technique is applied to observations taken during the Cirrus Regional Study of Tropical Anvils and Cirrus Layers–Florida Area Cirrus Experiment (CRYSTAL-FACE) campaign with the airborne Cloud Physics Lidar. The retrieved relative concentrations of particle shapes are compared with shape images from an airborne, in situ, cloud particle imager probe, operating in the same cloud. A first high-resolution time-based comparison, conducted over a short period of close collocation, leads to a good agreement between both techniques, with an average difference below 5% in retrieved relative concentrations. The same technique applied over the entire lifetime of three different convective ice clouds cases shows a maximum difference below 10% in average retrieved relative concentrations. The application of this technique to future spaceborne observations could lead to large-scale classification of particle shapes in ice clouds. **INDEX TERMS:** 0320 Atmospheric Composition and Structure: Cloud physics and chemistry; 3360 Meteorology and Atmospheric Dynamics: Remote sensing; 3374 Meteorology and Atmospheric Dynamics: Tropical meteorology; **KEYWORDS:** cirrus, microphysics, lidar

**Citation:** Noel, V., D. M. Winker, M. McGill, and P. Lawson (2004), Classification of particle shapes from lidar depolarization ratio in convective ice clouds compared to in situ observations during CRYSTAL-FACE, *J. Geophys. Res.*, 109, D24213, doi:10.1029/2004JD004883.

## 1. Introduction

[2] Ice clouds, also known as cirrus, cover permanently as much as 40% of the Earth's surface [Liou, 1986]. This significant presence makes them important actors in the climatic system, and a correct estimation of their radiative impact is essential to accurately reproduce and predict the climate evolution [Cess *et al.*, 1990]. To improve their parameterization in general circulation models, a better understanding of their microphysical properties is required [Stephens *et al.*, 1990; Sun and Shine, 1995]. Among these, the shape of ice particles remains one of the major sources of uncertainties, which could modify cirrus radiative impact by as much as 30% [Takano and Liou, 1989]. The modeled bidirectional reflectance of cirrus clouds is also highly sensitive to the assumed shape of ice crystals [Yang *et al.*, 2001], and using incorrect shapes for ice clouds in optical depth retrieval algorithms can modify results by a factor of 3 [Mishchenko *et al.*, 1996].

[3] Historically, cirrus cloud studies have focused on midlatitude areas, thanks to the high number of observation sites at these latitudes. However, recent studies and field

campaigns in tropical latitudes have focused on the frequent occurrence in these areas of large cloud systems created by fast convection processes. Because of their large horizontal and vertical extensions, these systems have a large-scale radiative impact on the planet surface and atmosphere [Hartmann *et al.*, 1992]. As they frequently extend up to the tropopause, their top layers can be composed of ice crystals several kilometers deep. Formation through rapid convection makes these ice clouds exhibit microphysical properties significantly different from midlatitude, synoptic cirrus, thus leading to a different radiative behavior [Heymsfield and Miloshevich, 1991; Knollenberg *et al.*, 1993; McFarquhar and Heymsfield, 1996; Heymsfield and McFarquhar, 1996]. Moreover, potential cloud radiative-convective feedback processes may lead to an increased greenhouse effect [Fowler and Randall, 1994]. Because of these potentially important implications for radiative budget, convective ice clouds are a major source of uncertainty in climate prediction. In order to acknowledge their differences with midlatitude cirrus clouds and the fact that it is often difficult to clearly separate convective ice clouds from the underlying cloud system, they will be referred to as ice clouds in the rest of this study.

[4] Tropical ice clouds are often generated at the tops of cumulonimbus clouds. These thick convective systems hide them from ground observation, meaning high-altitude observations are essential to the study of such clouds. In the near future, satellite lidars such as CALIPSO [Winker *et al.*, 2003] will provide this necessary data, with a special

<sup>1</sup>Analytical Services and Materials, Hampton, Virginia, USA.

<sup>2</sup>NASA Langley Research Center, Hampton, Virginia, USA.

<sup>3</sup>NASA Goddard Space Flight Center, Greenbelt, Maryland, USA.

<sup>4</sup>SPEC Inc., Boulder, Colorado, USA.

focus on ice cloud microphysical properties. The Cirrus Regional Study of Tropical Anvils and Cirrus Layers–Florida Area Cirrus Experiment (CRYSTAL-FACE) campaign was held in Florida during July 2002 (E. J. Jensen et al., Overview of the Cirrus Regional Study of Tropical Anvils and Cirrus Layers–Florida Area Cirrus Experiment (CRYSTAL-FACE), submitted to *Bulletin of the American Meteorological Society*, 2003) to provide comprehensive measurements needed to better understand the microphysical and radiative properties and formation processes of these clouds. Five midaltitude to high-altitude aircraft carried numerous in situ and remote sensing instruments, with simultaneous ground-based observations. The numerous collocated measurements allowed the development and validation of interinstrument synergies, giving new insights into the specific properties of tropical convective ice clouds. The present paper uses observations from CRYSTAL-FACE to compare particle shape classification retrieved from lidar depolarization ratio to measurements from in situ probes. Instruments used in this process and the shape classification itself are presented in section 2. Collocated detailed observations of a convective ice clouds are studied in section 3, and three complete data sets of convective ice clouds are studied in section 4. Discussion and conclusions are given in section 5.

## 2. Observations and Particle Shape Classification

### 2.1. Cloud Particle Imager

[5] The in situ observations used in the present paper were taken from a cloud particle imager (CPI) in situ probe mounted on the WB-57 aircraft, which was able to fly through the top of convective systems thanks to its high flight ceiling (up to 18 km). The CPI takes high-resolution images of cloud particles along the aircraft path [Lawson et al., 2001]. Particles are detected using two continuous-wave laser diodes with beams 2.4 mm wide and 0.5 mm thick. Laser beam intensities are constantly monitored by detectors on the opposite wall of the probe. The presence of a particle inside the sampling volume is detected by a decrease in the monitored laser intensities. It should be noted that the scattering of laser light induced by ice crystals can cause uncertainties during the particle detection phase. As the shape of small particles has a strong influence on light scattering, the lower limit of the probe particle size detection range can fluctuate. However, tests show that particles bigger than 50  $\mu\text{m}$  are reliably detected, and for each case studied a combination of particle size distributions from several probes will be used to evaluate the importance of big particles (section 3).

[6] Detection of a particle triggers the pulse of the imaging laser, which casts an image on a high-resolution CCD camera (2.3 microns pixel size). The cross sections are automatically analyzed to infer the shapes of cloud particles, taking into account such parameters as the particle projected surface area and dimensions. Shapes are classified into five major habits: spheroids, plates, small and big irregular habits, and columns. Shape concentrations are retrieved by relating shape percentages to particle size distributions and are averaged over 10-s time frames. To quantify the errors in this automatic process, a manual classification will be performed on a representative sample of data for each

case. Results are then compared to automatic retrievals to unveil any recurrent bias in the classification process.

### 2.2. Cloud Physics Lidar

[7] Thanks to its unique sensitivity to optically thin clouds, the lidar is one of the best suited instruments for the study of ice clouds [Platt, 1973]. The NASA Cloud Physics Lidar (CPL) is a three-wavelength (355 nm, 532 nm and 1064 nm) backscatter lidar [McGill et al., 2002]. Looking downward from the NASA ER-2 aircraft, it provided several days of observations from as high as 20 km, with a vertical resolution of 30 m. This configuration allowed unique monitoring of ice clouds located on top of tropical convective systems, which would be impossible from the ground because of the lower layers of thick water clouds blocking the lidar penetration. At the 1064 nm wavelength, the CPL provided observations of linear depolarization ratio  $\delta = I_{\perp}/I_{\parallel}$ , defined as the ratio of backscattered intensities in the planes of polarization perpendicular ( $I_{\perp}$ ) and parallel ( $I_{\parallel}$ ) to that of the linearly polarized source [Schotland and Stone, 1971]. Observations of parallel and perpendicular intensities were vertically averaged over 60 m, and profiles were averaged over 2 s to increase the signal-to-noise ratio before computing the depolarization ratio.

[8] The depolarization ratio  $\delta$  has been extensively studied using light-scattering simulations [Cai and Liou, 1982; Takano and Liou, 1989; Yang and Liou, 1996] and is primarily sensitive to the shape of particles in the probed cloud [Sassen, 1991]. In the present paper, results from a ray-tracing simulation (extensively described by Noel et al. [2001]) are compared to observations of  $\delta$  to retrieve particle shapes in ice clouds. The simulation follows modifications in light polarization as it travels through modeled hexagonal-based ice crystals, so the evolution of lidar depolarization ratio  $\delta$  can be studied as a function of three parameters: the particle imaginary index of refraction, orientation in space and aspect ratio.

[9] Unlike the real part of the refraction index, which is very stable in the wavelength range considered (355 to 1064 nm), the imaginary part goes through strong variations at these wavelengths. However, its values remains below  $10^{-6}$  [Warren, 1984], and Noel et al. [2001] showed that its effects on light polarization could be neglected. Moreover, horizontally oriented crystals, which are not uncommon in midlatitude and high-latitude ice clouds [Platt, 1977; Sassen, 1980], were shown to produce high backscattering and very low depolarization ratios ( $\delta < 0.1$ ) similar to those produced by water clouds, which is consistent with previous studies [Platt et al., 1978; Mishchenko et al., 1997]. When such low values are observed, the depolarization ratio is not sensitive to particle shape anymore, and the shape classification technique used in the present study cannot be applied. However, such low values are not observed in the present data set, so the random orientation required by the classification can be safely assumed for ice crystals observed in the present study. Finally,  $\delta$  appeared highly sensitive to the aspect ratio  $Q$  (Figure 1) in the presence of randomly oriented particles. As the slope of  $\delta(Q)$  is not always positive, it is not possible to link an observed  $\delta$  to a specific aspect ratio  $Q$ , but a range of possible values for  $Q$  can be estimated and crystals can be classified into three

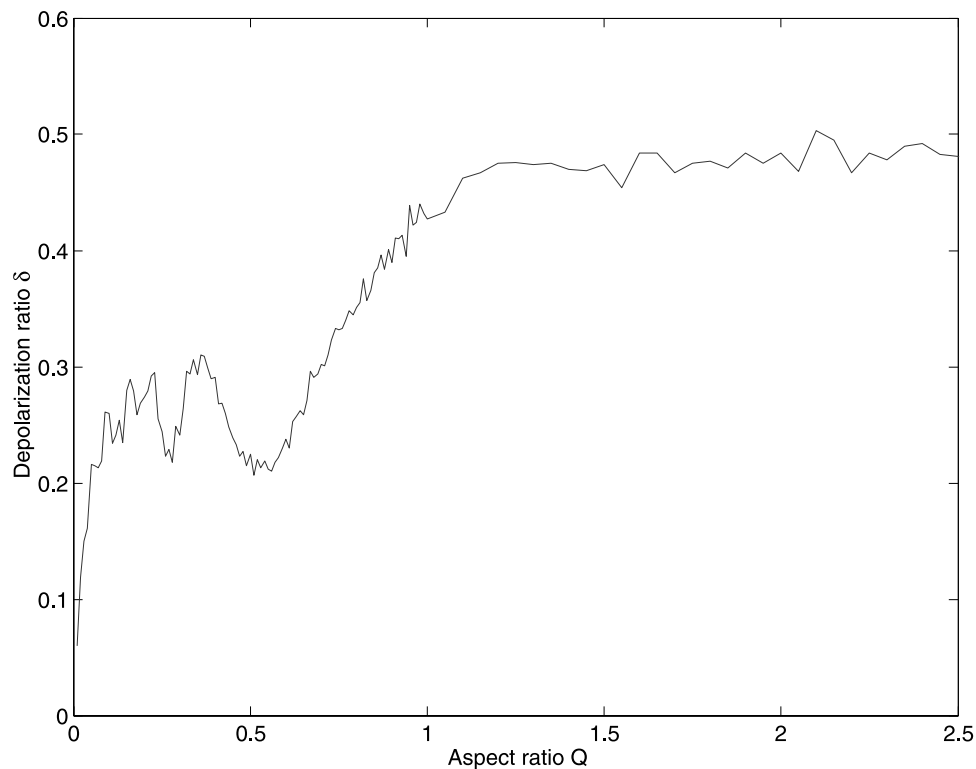


**Figure 1.** Evolution of linear depolarization ratio  $\delta$  for hexagonal-based ice particles with aspect ratios  $Q$  between 0.05 and 2.5 and effective radius of 50  $\mu\text{m}$ , at a wavelength of 1064 nm.

shape groups. Low values  $\delta < 0.25$  are attributed to thin platelike particles ( $Q < 0.1$ ), while high  $\delta > 0.5$  are found to be the signature of columnar crystals ( $Q > 1.5$ ). Experimental studies have found that spheroid particles produce low depolarization, in the same range as platelike particles, so these shapes will be equivalent in the lidar classification scheme. The last group describes intermediate and irregular particle shapes, which produce average depolarization ratios ( $0.25 < \delta < 0.5$ ). This technique was applied by Noel *et al.* [2002] on an extensive set of ground-based lidar observations of  $\delta$  in ice clouds. Results of shape classifications showed a good agreement with previous in situ studies in ice clouds [Korolev and Hallett, 2000; Sassen and Benson, 2001]. During this study, the potentially important effects of multiple scattering [Platt, 1973; Hu *et al.*, 2001] had to be taken into account by an additional simulation. For the present observations, however, the 100  $\mu\text{rad}$  CPL field of view gives a telescope spot size smaller than 1 m on most high clouds, so the multiple-scattering effects are kept at a minimum and can be safely ignored [Eloranta, 1998].

[10] The depolarization ratio can thus be used to classify particles in a given cloud area into distinct shape groups. As lidar observations are vertically resolved, the variability of shapes with altitude can be estimated.

### 2.3. Comparison of Particle Shape Classifications

[11] The goal of this paper is to compare particle shape classification in ice clouds from lidar depolarization ratio with collocated in situ observations from a cloud particle imager. Unfortunately, the lidar depolarization ratio cannot classify particle shapes into five habits like the CPI (section 2.1). Thus particles have to be regrouped into

more general shape classes: Thin plates or spheroids give similar low depolarization ratios (section 2.2), so these shapes will be regrouped as the first class. Moreover, as lidar depolarization ratio does not depend on particle size in first approximation, big and small irregular particles cannot be distinguished through depolarization ratio and will be regrouped in a second class. The last class will describe columns, which can be equally identified by either instrument.

### 3. A Convective Ice Cloud Case Study: 29 July

[12] During the campaign, several small-scale convective systems developed and dissipated during single days, extending horizontally over 100 km. The upper part of these anvil systems can extend higher than 15 km, leading to top layers mostly composed of ice crystals. On 29 July, one of these systems developed and dissipated between 1600 and 2300 UTC. It was targeted and monitored by the CRYSTAL-FACE aircraft between 1800 and 2100 UTC, at the middle of its life cycle. During this time frame, the system extended from near the ground up to 14 km, and at its widest the horizontal extension was greater than 150 km.

[13] CPI observations were conducted for several periods of time inside the cloud, for a total of 24 min. During this time period, a composite size spectra was derived from combined measurements of two probes on the WB-57: Scattering Spectrometer Probe (SPP-100), 4–60  $\mu\text{m}$ , and Cloud, Aerosol and Precipitation Spectrometer (CAPS), 0.5–44  $\mu\text{m}$  and 75–1600  $\mu\text{m}$  [Baumgardner *et al.*, 2001]. Results show that particles bigger than 50  $\mu\text{m}$  account for 43.14% of all optical cross sections (Figure 2). During 61%

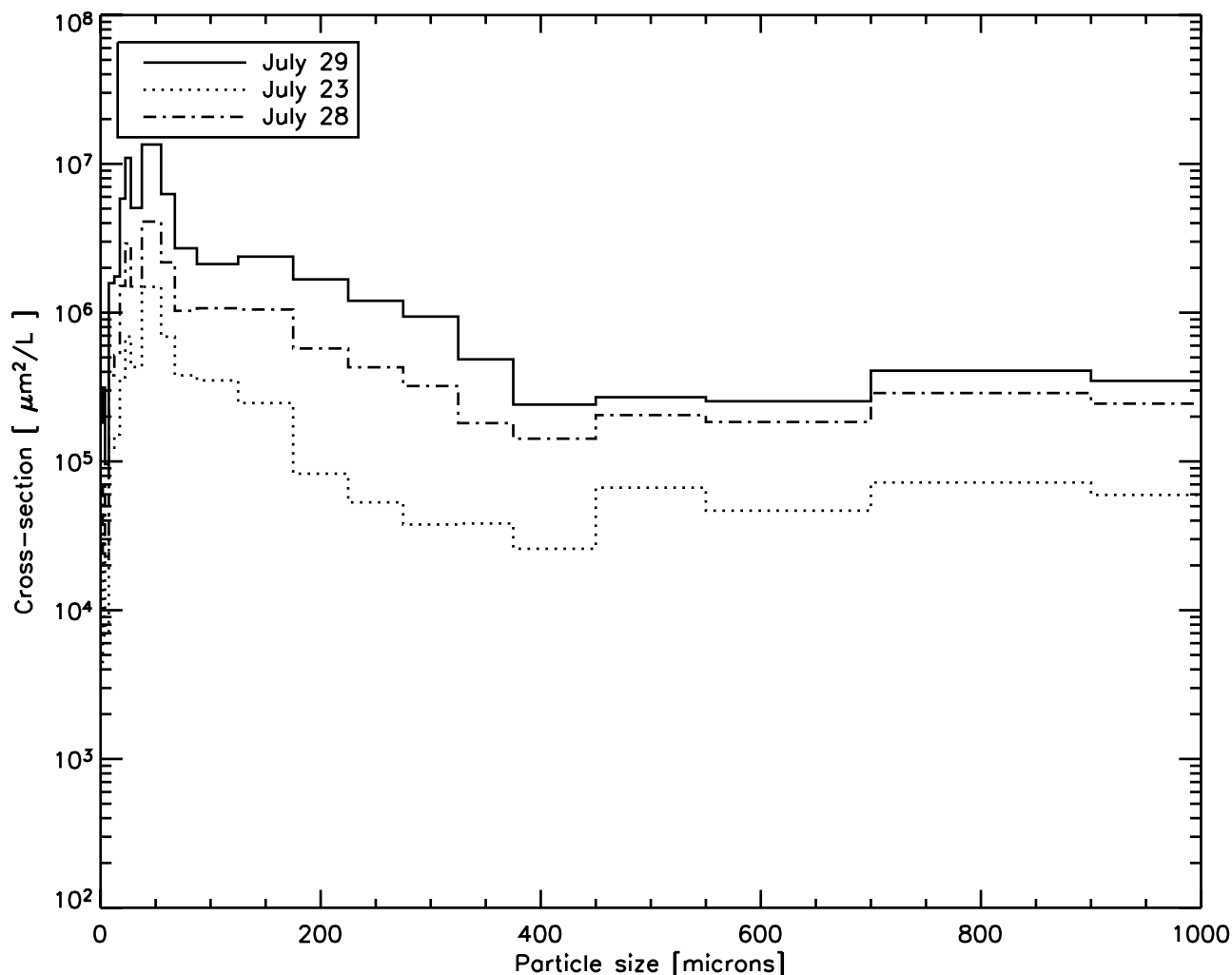


**Figure 2.** Distribution of optical cross sections as a function of particle size for each case, based on combined measurements from CAPS, CPI and SPP-100 probes, in  $\mu\text{m}^2/\text{L}/\mu\text{m}$ .

of this period, the WB-57 was out of the range of lidar penetration, so a time-dependent comparison of shape classification over this whole data set would lead to high uncertainties. However, between 1953:24 and 1954:48 UTC the WB-57 reached a low-altitude area of the convective system and got inside the region observed by the CPL (Figure 3a). The horizontal distance between the WB-57 and the ER-2 stayed below 1 km; hence observations from instruments on both platforms are considered collocated.

[14] An excerpt of CPI observations (Figure 4) shows the variety of possible crystal shapes, highlighting the complexity of shape classification. CPI concentrations, averaged over the whole collocated time frame, show more than 60% irregular shapes (diamond symbols in Figure 5), followed by 33% plates and spheroids (star symbols) and finally a low concentration of columns ( $\sim 7\%$ , square symbols). All these concentrations are relatively stable along the flight track, with only a slight increase ( $\sim 5\%$ ) in irregular habit concentration, with a simultaneous decrease in plates and spheroids. Manual shape classification was performed on a stable subset (441 particles) of this CPI data to quantify the errors in automatic shape recognition. Even if the number of particles for a given habit sometimes shows significant

differences, the final relative concentrations are very close to automatic classification (Table 1), with the biggest difference for irregular shapes: Automatic classification overestimates their relative concentration by  $\sim 3.17\%$ . Plates and spheroids are underestimated by less than 2%, just as columns.

[15] During the collocated time frame, the lidar was able to penetrate the higher, optically thin layers: Depolarization ratio  $\delta$  was observed between 14 km and 11 km, depending on the cloud top altitude, with observations available for an average 1 km range below cloud top (Figure 3a). The average profile of  $\delta$  is relatively constant with altitude (Figure 3b), with a standard deviation (shown in grey) of 0.17 in average. The absence of data below 12 km in Figure 3 is due to the lidar signal dropping below the noise threshold. The actual cloud base was much lower, as collocated radar observations show.

[16] Values of  $\delta$  were extracted from CPL profiles 500 m above and below the WB-57 altitude. Each  $\delta$  data point was converted into one of three shape habits (section 2.2), and the distribution of habits among these points was used to estimate the relative concentration of each shape. Results are very consistent with the CPI measurements (black lines

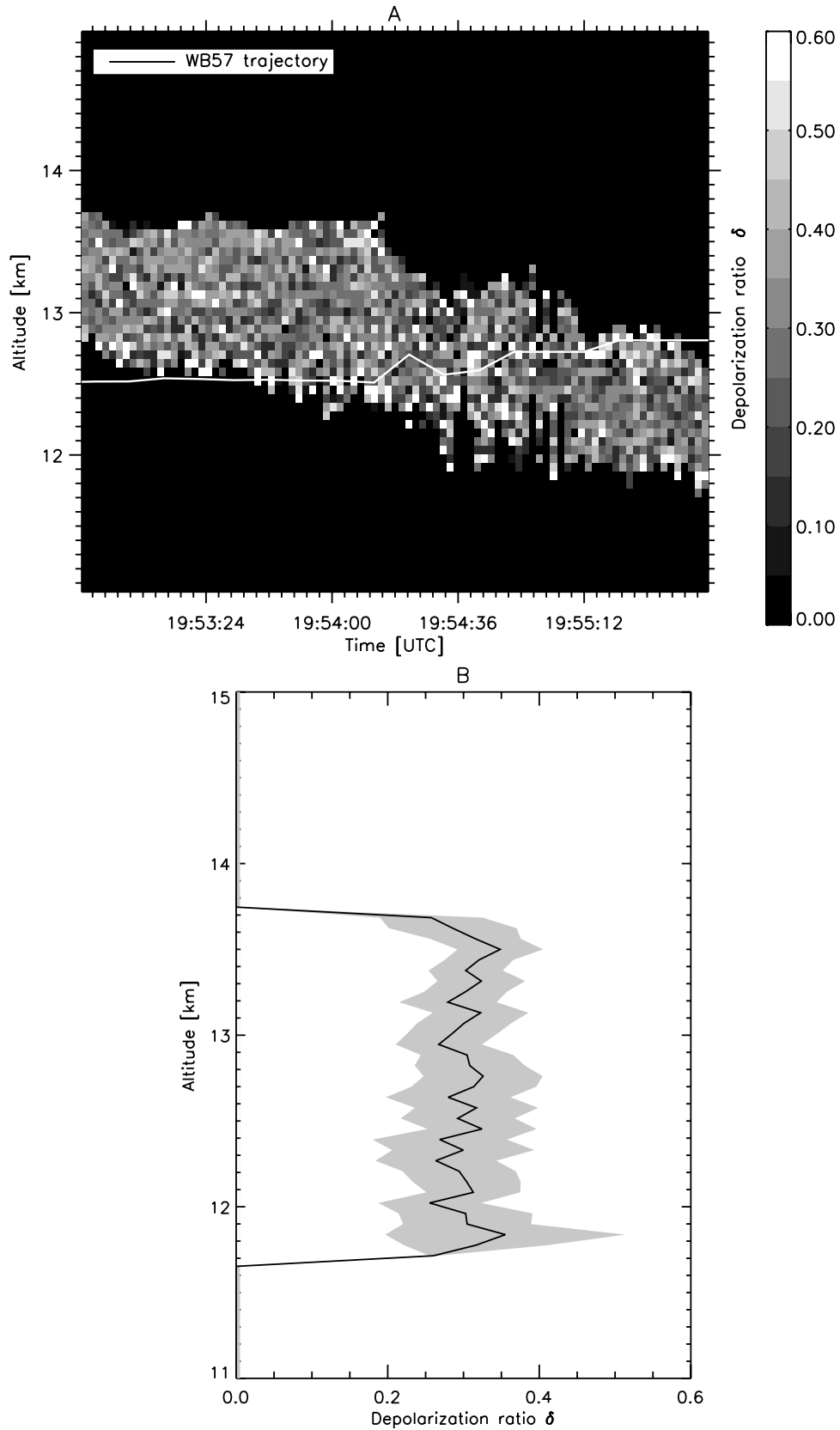


**Figure 3.** (a) CPL depolarization ratio at coincident points with WB-57 for the 29 July convective cirrus case at 1064 nm. (b) Same data averaged over the observation time frame, with standard deviation shown by the grey area. The cloud system extends to the ground, but the limited lidar penetration depth prevents cloud observation below 12 km.



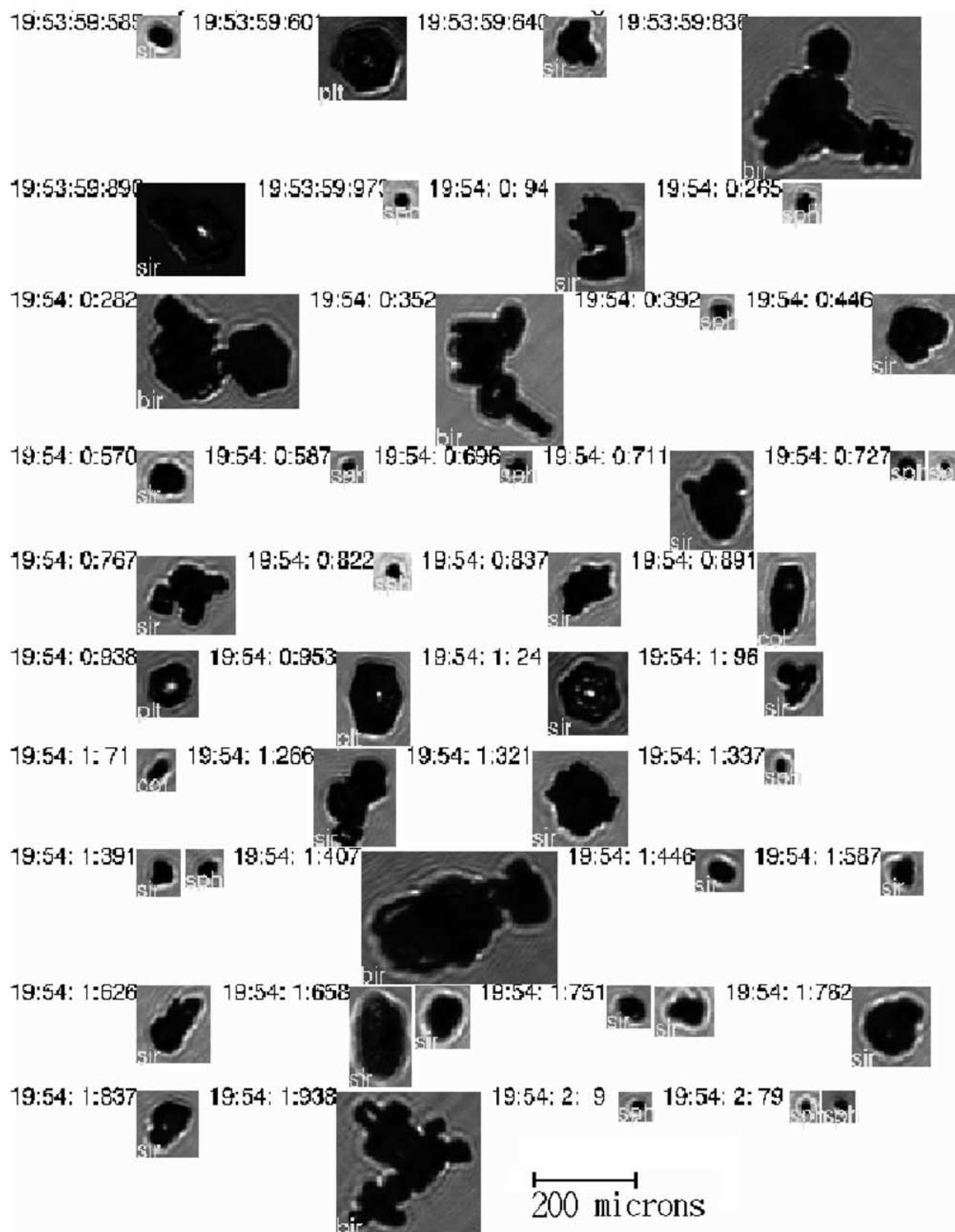


**Figure 4.** Example of CPI observations for the 29 July convective cirrus case. Particles are classified as spheroids ("sph"), plates ("pla"), small and big irregular habits ("sir" and "bir") or columns ("col").

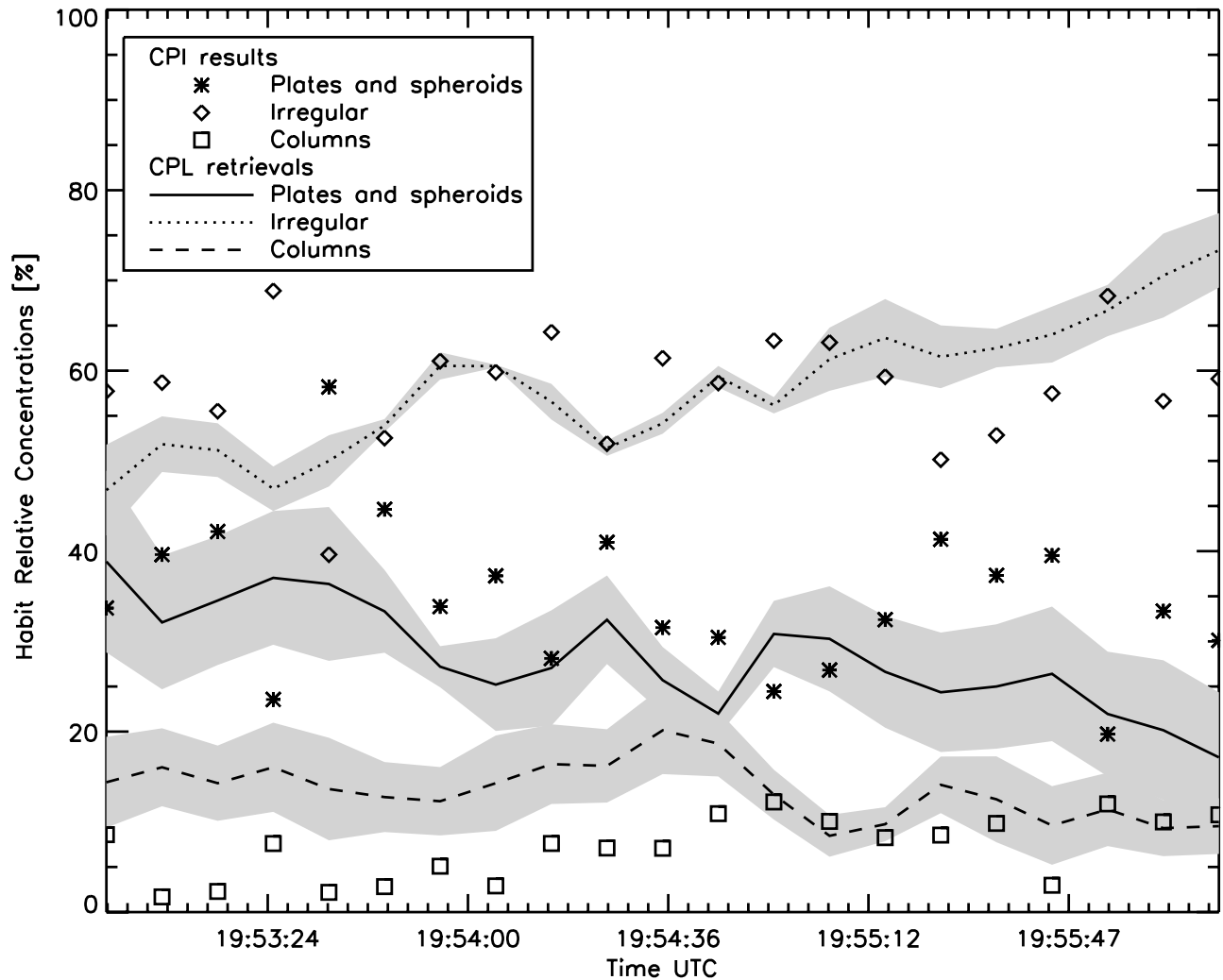


**Figure 5.** Evolution of habit percentages from CPI with time, compared to lidar retrievals for the 29 July convective cirrus case.

in Figure 5). The grey area shows the uncertainty for retrieved concentrations, due to the finite signal-to-noise ratio of the depolarization ratio  $\delta$ . As irregular shapes cover the broadest range of  $\delta$  values (section 2.2), small variations of  $\delta$  will have a small impact on retrieved concentrations for these shapes. That is consistent with the uncertainties, which are smaller for irregular habits (5.0% in average) and higher for plates and spheroids (12.2% in average), with 7.9% in average for columns. The maximum difference between observed and retrieved concentrations occurs for columns (dashed lines), which are overestimated ( $\sim 15\%$  for CPL retrievals and  $\sim 5\%$  for CPI observations) before 1954 UTC.

[17] During the collocated time frame, the WB-57 went from an altitude of 12.5 km to 13.2 km. The measured CPI habit concentrations were averaged over 100-m altitude bins and plotted as a function of altitude (symbols in Figure 6). Overall, shape concentrations are stable with altitude. Irregular shapes are dominant ( $\sim 60\%$ , diamond symbols) with a concentration increasing by 10% from 12.7 to 13.2 km, following the trend observed in Figure 5. Concentrations of plates and spheroids remain stable (25 to 36%, star symbols), with columns following the same behavior (less

than 10%, square symbols). Retrieved shape percentages from CPL depolarization ratios for correlated observation points, averaged in the same altitude ranges, are shown as black lines in Figure 6, with the grey area quantifying the uncertainties. The concentration of columns is still overestimated, but on the other hand, the increase in irregular habits with altitude (dotted lines) is highly correlated. This almost perfect alignment is most likely an artifact of the visual representation, as it is not apparent in time-based comparisons (Figure 5). Overall, however, the trends in CPI data are closely reproduced by the CPL retrievals, and most CPI concentrations are contained in the area defined by the CPL uncertainties. These differ slightly from the time-based results (Figure 5), because of the different grouping of

**Table 1.** Particle Shape Relative Concentrations From CPI Observations, for a Stable Subset of the 29 July Case<sup>a</sup>

	Plates and Spheroids	Irregular Habits	Columns
Automatic	27.4%	67.1%	5.4%
Manual	29.2% (+1.8%)	63.9% (−3.2%)	6.8% (+1.4%)

<sup>a</sup>The variation of concentrations from automatic to manual classification is noted in parentheses.

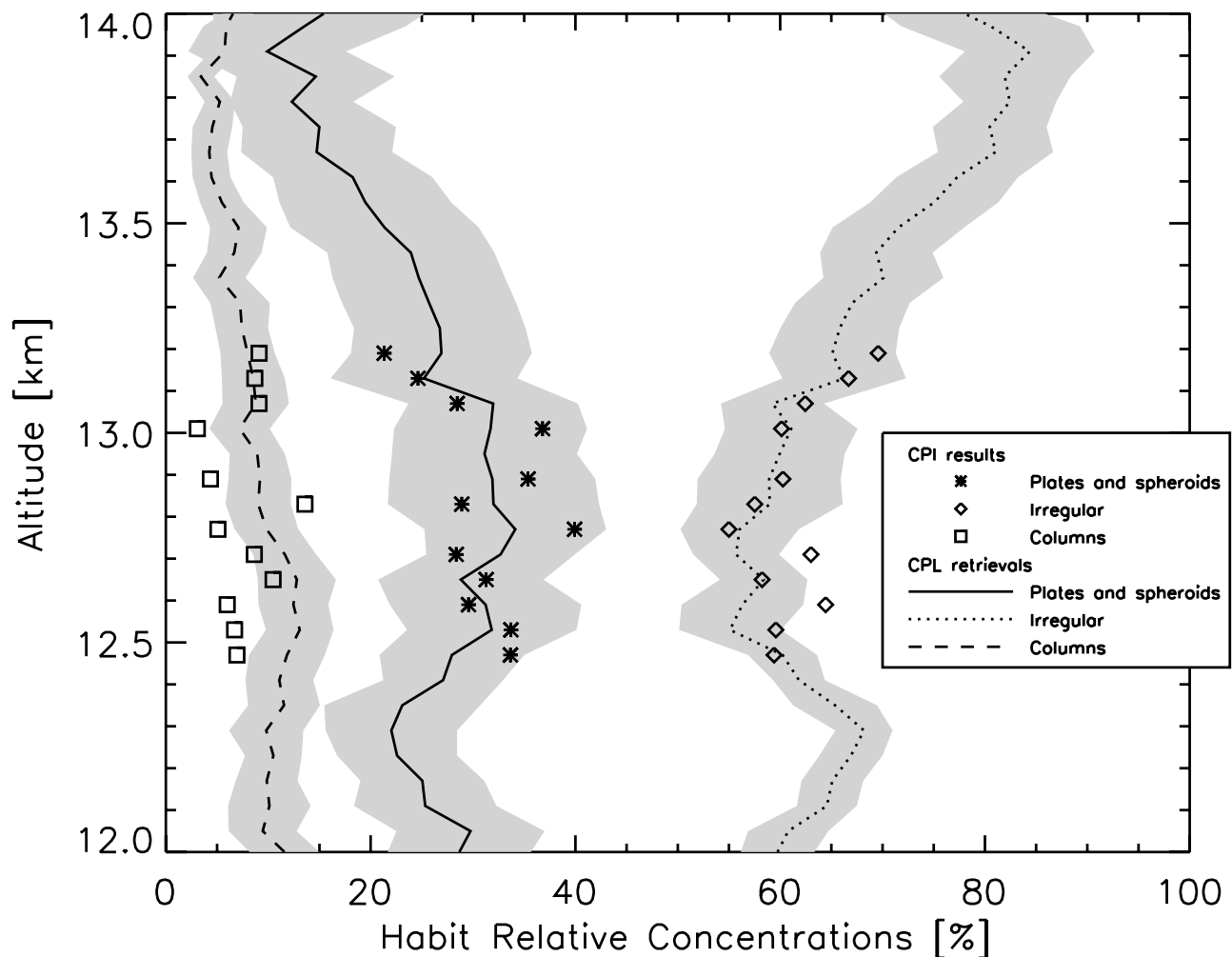


**Figure 6.** Evolution of habit percentages from CPI with altitude, compared to lidar retrievals for the 29 July convective cirrus case.

analyzed depolarization ratio, with the highest uncertainties for plates (grey area, 12.1% on average), the smallest for columns (4.3% on average), and 9.4% for irregular habits. Lidar retrievals outside the WB-57 altitude range suggest that irregular shape concentration increases up to 80% at 14 km, while the concentration of plates gradually falls to  $\sim 15\%$ . This information would not be accessible with CPI data alone and highlights the capacity of lidars to retrieve complete profiles of habit percentages, however limited by their penetration depth.

#### 4. Results for Three Cases

[18] The same analysis is conducted on the remaining 24 min of temporally overlapping CPI and CPL observations on 29 July and on two other cases of convective systems, 23 and 28 July and (Table 2). The 23 July case developed around 1900 UTC and was observed for its entire lifetime until it dissipated around 2330 UTC. This case has the lowest cloud top average altitude (12.1 km, Table 2) with the highest standard deviation (1.61). The 28 July case developed between 1900 and 2000 UTC and was monitored from 2100 UTC to its dissipation around 2300 UTC. Lidar observations of depolarization ratio  $\delta$  are shown in

Figures 7a and 7b for a single pass over these two cloud systems. Lidar penetration depth is similar for all cases, ranging between 0.83 km (29 July) and 1.2 km (23 and 28 July), which implies similar volume extinction coefficients and particle concentrations among cases. The CPL was able to penetrate the observed cloud system below the WB-57 altitude more than 98% of the time for the 23 and 28 July and cases (Table 2).

#### 4.1. Comparison of Shape Classifications

[19] The WB-57 followed the cloud altitudes; hence variations in the plane average altitudes mirror the cloud

**Table 2.** Summary of the Properties of Cirrus Cloud Cases Studied

	23 July	28 July	29 July
Lidar cloud top, km	$12.1 \pm 1.6$	$14.1 \pm 0.8$	$13.4 \pm 0.6$
WB-57 average altitude, km	$11.8 \pm 2.3$	$13.0 \pm 1.3$	$12.6 \pm 0.3$
Lidar penetration, km	$1.2 \pm 0.7$	$1.2 \pm 0.5$	$0.8 \pm 0.2$
CPI observation time (in CPL zone)	17 min (98%)	38 min (98%)	24 min (61%)
Temperature range, °C	−53.5, −43.1	−67.8, −58.1	−61.3, −55.9



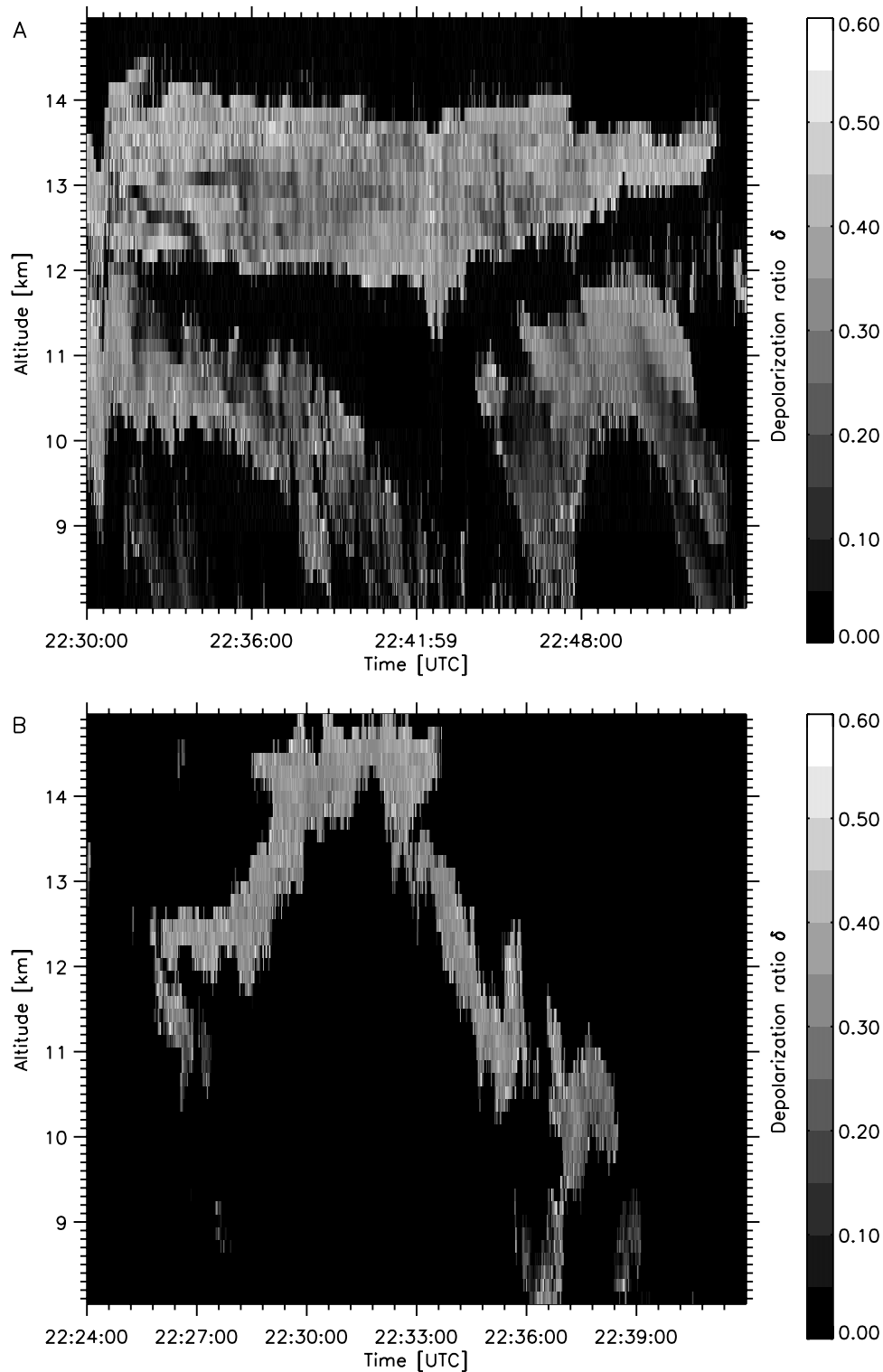


**Figure 7.** Depolarization ratio observations from the CPL for one ER-2 flight leg over the convective system for (a) 23 July case and (b) 28 July case. The cloud system extends to the ground, but the limited lidar penetration depth prevents observation of cloud base.

top variations. Intermittent CPI observations were conducted during each case, with total observation time ranging between 17 min (for 23 July case) and 38 min (for 28 July, Table 2). Composite size spectra (Figure 2) for these two cases show that particles bigger than 50  $\mu\text{m}$  account for

48.68 and 49.71% of all particle optical cross sections, respectively.

[20] For each case, habit retrievals from the CPI are very stable with time and are shown in black in Figure 8a (23 July), Figure 8b (28 July) and Figure 8c (29 July).

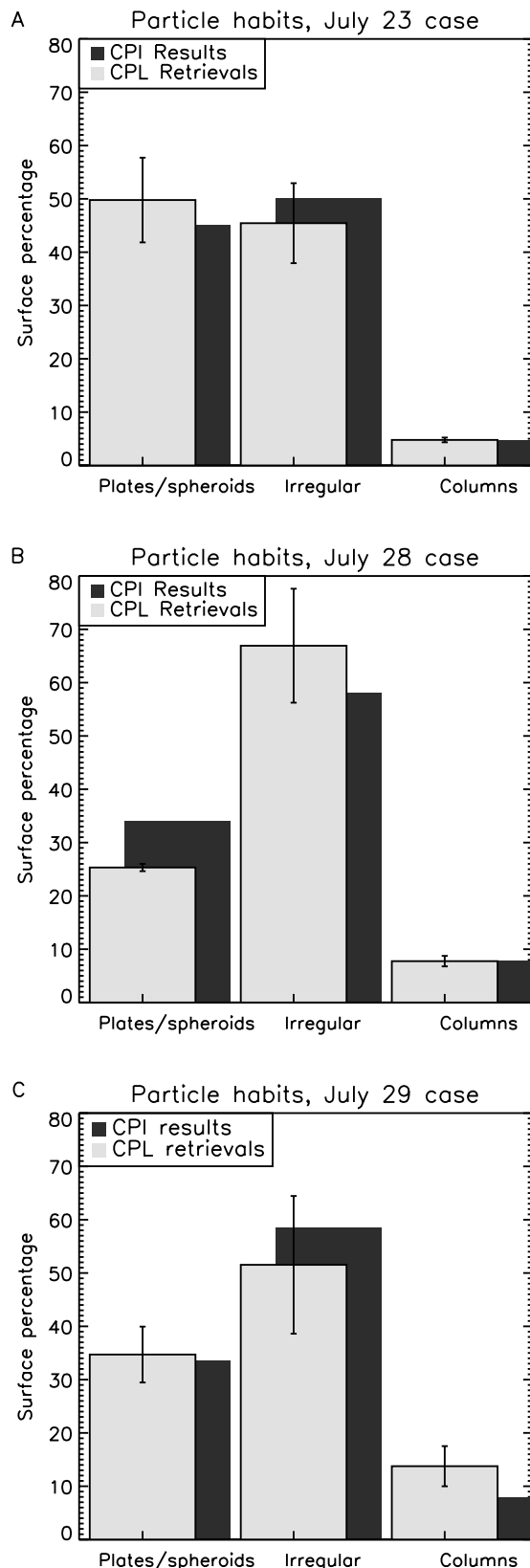


**Figure 8.** Habit percentages from CPI compared to lidar retrievals for three CRYSTAL-FACE convective cirrus cases.

Habit concentrations are similar for the 28 July (Figure 8b) and 29 July cases (Figure 8c): a strong majority of irregular particles ( $\sim 60\%$ ), followed by plates and spheroids (33–35%), and a minority of columns (5–7%). For the 23 July case, the overall cloud altitude is lower, meaning a higher temperature, so different microphysical properties should be expected. Retrieved concentrations are consistent (Figure 8a), showing higher concentrations of plates and spheroids ( $\sim 45\%$ ) and lower concentrations of irregular habits ( $\sim 50\%$ ) than for other cases. To quantify the errors in automatic shape retrieval, a manual classification was conducted on stable subsets in each case. As the sampled data set is not the same, the resulting concentrations, shown in Table 3, are slightly different from total averages (Figure 8) and should only be considered as validation. The biggest variation is observed for irregular particles, which are overestimated by less than 3% in all cases. Manual classification reveals that these wrongly identified particles are equally distributed among plates, spheroids and columns, which are underestimated by the automatic processing. In the end, variation stays below 3%, and the results of automatic classification are very close to manual findings.

[21] CPL observations were selected for the horizontal distance between the WB-57 and the ER-2 below 10 km, and depolarization ratios  $\delta$  were extracted at altitude levels close to the WB-57. Particle shape classification was conducted on these CPL observations following the process described in section 3. Retrieved relative concentrations are consistent with CPI observations (Figure 8, in grey), with the order of dominant shapes correctly identified in all cases and a difference below 7% between the average CPI concentrations and CPL retrievals. Uncertainties due to variability in  $\delta$  are low in all cases for columns (less than  $\pm 4\%$ ) and are generally lower than  $\pm 10\%$ , the maximum value of  $\pm 15\%$  reached for irregular habits in the 29 July case. The retrieved percentages are especially close to CPI observations for columnar shapes, which moreover show very low uncertainties.

#### 4.2. Temperature Profiles of Average Concentrations

[22] Shape classification was applied to all lidar observations of depolarization ratio  $\delta$  for the three cases (more than 16 hours). Vertical profiles of retrieved shape percentages against atmospheric temperature (Figure 9) show an expected dependence on temperature [Pruppacher and Klett, 1997]: The relative concentration of plates and spheroids decreases from  $\sim 65\%$  at  $-20^\circ\text{C}$  to less than 20% below  $-75^\circ\text{C}$ , while the relative concentration of irregular-shaped particles increases from  $\sim 35\%$  to more

**Table 3.** Particle Shape Relative Concentrations From CPI Observations, for a Stable Subset of All Cases<sup>a</sup>

Case	Processing	Plates and Spheroids	Irregular	Columns
July 23	automatic	44.2%	53.8%	2.0%
	manual	44.6% (+0.4%)	52.8% (−1%)	2.6% (+0.6%)
July 28	automatic	26.5%	68.4%	5.1%
	manual	28.6% (+2.1%)	65.7% (−2.7%)	5.7% (+0.6%)
July 29	automatic	26.4%	68.5%	5.1%
	manual	28.2% (+1.8%)	65.5% (−3%)	6.3% (+1.2%)

<sup>a</sup>The variation of concentrations from automatic to manual classification is noted in parentheses.

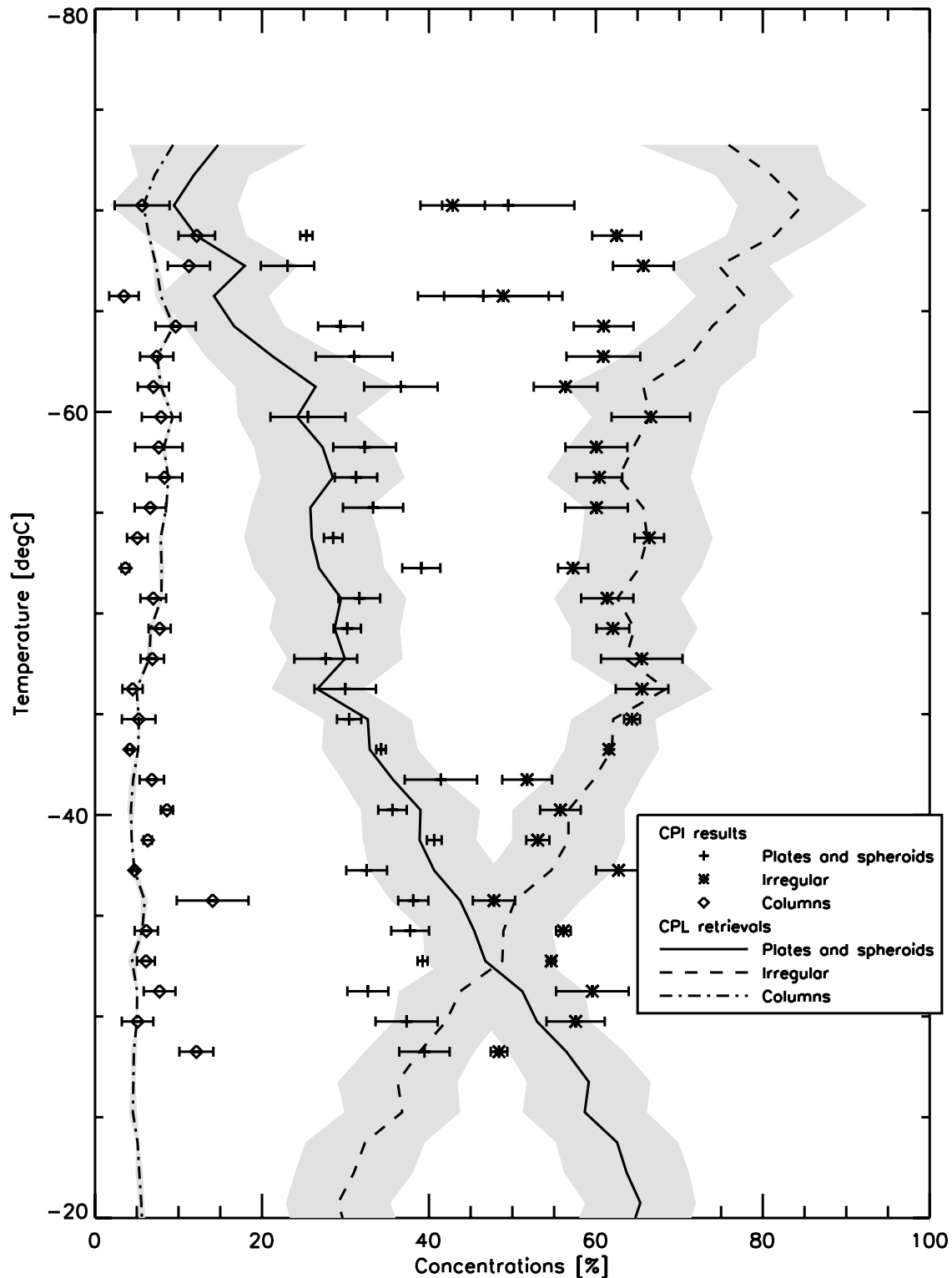


**Figure 9.** Habit percentages from CPI compared to lidar retrievals for the three cases, averaged as a function of temperature.

than 75%. Rather surprisingly, the concentration of columns stays very stable with temperature, with only a small increase from 5 to 10% from  $-20^{\circ}\text{C}$  to  $-75^{\circ}\text{C}$ . This is different from most observations in synoptic cirrus clouds at midlatitudes, in which top layers usually show high concentrations of columns and polycrystals [Baran *et al.*, 1999;

Chepfer *et al.*, 2001; Noel *et al.*, 2002]. Columns concentrations retrieved by lidar analysis are also very stable considering the variability of  $\delta$ : Uncertainties are very low (less than 5%).

[23] Relative concentrations from CPI observations over the three cases were gathered as a function of atmospheric

temperature and averaged over 1.5°C bins (symbols in Figure 9). Error bars show the standard deviation of observed concentrations in the temperature interval studied. The agreement is good between CPI observations and CPL retrievals: The order of dominant shapes is consistent, and the evolution of concentrations with temperature is consistently reproduced with both techniques. The best agreement is reached for temperatures between  $-60^{\circ}\text{C}$  and  $-35^{\circ}\text{C}$  (53.9% of observations). Below  $-60^{\circ}\text{C}$  (40.2% of observations), concentrations of plates and spheroids are underestimated by less than 10%, while irregular habits are overestimated by as much as 20%. Above  $-35^{\circ}\text{C}$  (5.9% of observations), these differences are reversed: Concentrations of plates and spheroids are overestimated, and irregular habits are underestimated by less than 10%. On the other hand, retrieved concentrations of columns are very stable. The fact that both techniques consistently reproduce this unusual stability confirms that this tendency is not due to instrumental biases but is rather a specific microphysical property of the studied cases of convective ice clouds.

## 5. Discussion and Conclusion

[24] The present paper compares shape classification retrieved from lidar depolarization ratio to actual observations from a cloud particle imager. A limited data set from a selected time frame of closely collocated convective ice clouds observations from lidar and CPI was used from the CRYSTAL-FACE campaign (section 3). Comparison of shape classifications for this data set shows a good agreement with the CPI observations (section 4). Uncertainties are lower than 13%.

[25] Moreover, observations from three cases of convective cloud systems were used in their entirety (section 4). The WB-57 is generally within the CPL penetration depth, and a good agreement is found overall between retrieved shapes percentages. In all comparisons, the order of importance of shape classes is correctly identified, and the retrieved percentage of columns is similar to CPI results with an average difference of 3% in retrieved concentrations. The maximum difference in shape percentages is less than 10% in all cases, and uncertainties for retrievals are below 15%. Considering that the CPI detection is only accurate for particles bigger than  $\approx 50\text{ }\mu\text{m}$  and that these particles account for 43.1–49.7% of optical cross sections, the variation between the results of both classifications could be caused by a small variation in shape distribution with particle size. The averaged vertical profiles of retrieved particle shapes (section 4.2) show that with the exception of column particles, the difference between CPI-observed and CPL-retrieved concentrations increases with low temperatures (Figure 9). This difference could come from a misclassification of irregular habits as spheroids or platelike particles in CPI observations or from the presence of thick plates in the upper layers of the ice clouds studied, which would lead to high depolarization ratios, which would wrongly classify them as irregular habits during the CPL analysis.

[26] Even if results are very consistent with actual observations, lidar observations have their own inherent limitations. First of all, only the upper, optically thin cloud layers can be analyzed through the lidar technique. This problem is

generally avoided, as this technique is aimed at the study of ice clouds, which are optically thin. Moreover, observations from space lidars could present a lower signal-to-noise ratio, which could potentially lead to high uncertainties in the retrieved shape class frequencies. Finally, the lidar sampling volume can be quite large, and mixtures of different shapes could lead to an averaging of depolarization ratio and thus to biases in the classification results. However, these mixtures would have to be homogeneous on scales inferior to the lidar resolution ( $\approx 15\text{ m}$ ), and the in situ observations used in the present paper do not show such particular properties; thus they seem unlikely.

[27] Another limitation to the technique lies in the nature of retrieved values: The particle habit concentrations retrieved from CPL observations can only be relative. Lidar backscattered intensity, when combined with external observations, like radar reflectivity, can complete this information by estimating concentrations and particle size distribution [Donovan *et al.*, 2001]. Finally, retrievals in the present paper suggest that the majority of particles adopt irregular shapes, which are extremely variable. As it is still unclear how the microphysical properties of an ice cloud drive its radiative properties, the variations of shapes inside the irregular category alone could have a great influence on the cloud radiative properties. This highlights the limitations of a classification into arbitrary canonical shapes. A departure from the habit model would require a different approach, for example, a classification using shape-sensitive parameters like the area ratio [Heymsfield and Miloshevich, 2003].

[28] In order to proceed with the comparison, the number of identifiable shape classes from lidar retrievals was set to three. This is less than the five habits measured from CPI (section 2.1) and may seem too simple when compared to the infinity of different shapes found in ice clouds. However, in the absence of relevant information, most climate simulations still assume fixed or arbitrarily distributed shapes in ice clouds. Once applied to large-scale observations from future satellite experiments, such as the CALIPSO mission, this technique could solve this uncertainty and give valuable insight into particle shape habits in ice clouds, specifying their evolution with latitudes and geographical location. This classification would be a great help in the evaluation of the radiative impact of ice clouds.

## References

- Baran, A. J., S. J. Brown, J. S. Foot, and D. L. Mitchell (1999), Retrieval of tropical cirrus thermal optical depth, crystal size and shape using a dual view instrument at 3.7 mm and 10.8 mm, *J. Atmos. Sci.*, **56**, 92–110.
- Baumgardner, D., H. Jonsson, W. Dawson, D. O'Connor, and R. Newton (2001), The cloud, aerosol and precipitation spectrometer: A new instrument for cloud investigations, *Atmos. Res.*, **59–60**, 251–264, doi:dx.doi.org/10.1016/S0169-8095(01)00119-3.
- Cai, C., and K. N. Liou (1982), Polarized light scattering by hexagonal ice crystals: Theory, *Appl. Opt.*, **21**(19), 3569–3580.
- Cess, R. D., et al. (1990), Intercomparison and interpretation of climate feedback processes in 19 atmospheric general circulation models, *J. Geophys. Res.*, **95**, 16,601–16,615.
- Chefer, H., P. Goloub, J. Riedi, J. D. Haan, J. W. Hovenier, and P. Flamant (2001), Ice crystal shapes in cirrus clouds derived from POLDER/ADEOS-1, *J. Geophys. Res.*, **106**, 7955–7966.
- Donovan, D. P., et al. (2001), Cloud effective particle size and water content profile retrievals using combined lidar and radar observations: 2. Comparison with IR radiometer and in situ measurements of ice clouds, *J. Geophys. Res.*, **106**, 27,449–27,464.

- Eloranta, E. W. (1998), Practical model for the calculation of multiply scattered lidar returns, *Appl. Opt.*, **37**(12), 2464–2471.
- Fowler, L. D., and D. A. Randall (1994), A global radiative convective feedback, *Geophys. Res. Lett.*, **21**, 2035–2038.
- Hartmann, D. L., M. E. Ockert-Bell, and M. L. Michelsen (1992), The effect of cloud type on earth's energy balance: Global analysis, *J. Clim.*, **5**, 1281–1304.
- Heymsfield, A. J., and G. M. McFarquhar (1996), On the high albedos of anvil cirrus in the tropical pacific warm pool: Microphysical interpretations from cepep and from kwajalein, marshall islands, *J. Atmos. Sci.*, **53**, 2401–2423.
- Heymsfield, A. J., and L. M. Miloshevich (1991), Limit to greenhouse warming?, *Nature*, **351**, 14–15.
- Heymsfield, A. J., and L. M. Miloshevich (2003), Parameterizations for the cross-sectional area and extinction of cirrus and stratiform ice cloud particles, *J. Atmos. Sci.*, **60**, 936–956.
- Hu, Y. X., D. Winker, P. Yang, B. Baum, L. Poole, and L. Vann (2001), Identification of cloud phase from PICASSO-CENA lidar depolarization: A multiple scattering sensitivity study, *J. Quant. Spectrosc. Radiat. Transfer*, **70**, 569–579.
- Knollenberg, R. G., K. Kelly, and J. C. Wilson (1993), Measurements of high number densities of ice crystals in the tops of tropical cumulonimbus, *J. Geophys. Res.*, **98**, 8639–8664.
- Korolev, A., and G. A. I. J. Hallett (2000), Ice particle habits in stratiform clouds, *Q. J. R. Meteorol. Soc.*, **126**, 2873–2902.
- Lawson, R. P., B. A. Baker, C. G. Schmitt, and T. L. Jensen (2001), An overview of microphysical properties of Arctic clouds observed in May and July 1998 during FIRE ACE, *J. Geophys. Res.*, **106**, 14,989–15,014.
- Liou, K. N. (1986), Influence of cirrus clouds on weather and climate processes: A global perspective, *Mon. Weather Rev.*, **114**, 1167–1199.
- McFarquhar, G., and A. J. Heymsfield (1996), Microphysical characteristics of three cirrus anvils sampled during the Central Equatorial Pacific Experiment (CEPEX), *J. Atmos. Sci.*, **52**, 2401–2423.
- McGill, M. J., D. L. Hlavka, W. D. Hart, J. D. Spinhirne, V. S. Scott, and B. Schmid (2002), The Cloud Physics Lidar: Instrument description and initial measurement results, *Appl. Opt.*, **41**, 3725–3734.
- Mishchenko, M. I., W. B. Rossow, A. Macke, and A. A. Lacis (1996), Sensitivity of cirrus cloud albedo, bidirectional reflectance and optical thickness retrieval accuracy to ice particle shape, *J. Geophys. Res.*, **101**, 16,973–16,985.
- Mishchenko, M. I., D. J. Welaard, and B. E. Carlson (1997), T-matrix computations of zenith-enhanced lidar backscatter from horizontally oriented ice plates, *Geophys. Res. Lett.*, **24**, 771–774.
- Noel, V., H. Chepfer, G. Ledanois, and P. H. Flamant (2001), Computation of a single-scattering matrix for nonspherical particles randomly or horizontally oriented in space, *Appl. Opt.*, **40**, 4365–4375.
- Noel, V., H. Chepfer, G. Ledanois, A. Delaval, and P. H. Flamant (2002), Classification of particle shape ratios in cirrus clouds based on the lidar depolarization ratio, *Appl. Opt.*, **41**, 4245–4257.
- Platt, C. (1973), Lidar and radiometric observations of cirrus clouds, *J. Atmos. Sci.*, **30**, 1191–1204.
- Platt, C. M. R. (1977), Lidar observations of a mixed-phase altostratus cloud, *J. Appl. Meteorol.*, **16**, 339–345.
- Platt, C. M. R., N. L. Abshire, and G. T. McNice (1978), Some microphysical properties of an ice cloud from lidar observations of horizontally oriented crystals, *J. Appl. Meteorol.*, **17**, 1220–1224.
- Pruppacher, H. R., and J. D. Klett (1997), *Microphysics of Clouds and Precipitation*, 914 pp., Springer, New York.
- Sassen, K. (1980), Remote sensing of planar ice crystals fall attitude, *J. Meteorol. Soc. Japan*, **58**, 422–433.
- Sassen, K. (1991), The polarization lidar technique for cloud research: A review and current assessment, *Bull. Am. Meteorol. Soc.*, **71**, 1848–1866.
- Sassen, K., and S. Benson (2001), A midlatitude cirrus cloud climatology from the facility for atmospheric remote sensing. Part II: Microphysical properties derived from lidar depolarisation, *J. Atmos. Sci.*, **58**, 2103–2111.
- Schotland, R. M., and R. J. Stone (1971), Observations by lidar of linear depolarization ratios by hydrometeors, *J. Appl. Meteorol.*, **10**, 1011–1017.
- Stephens, G. L., S.-C. Tsay, P. W. Stackhouse, and P. J. Flatau (1990), The relevance of the microphysical and radiative properties of cirrus clouds to climate and climate feedback, *J. Atmos. Sci.*, **47**, 1742–1753.
- Sun, Z., and K. P. Shine (1995), Parameterization of ice cloud radiative properties and its application to the potential climatic importance of mixed-phased clouds, *J. Clim.*, **8**, 1874–1888.
- Takano, Y., and K. N. Liou (1989), Solar radiative transfer in cirrus clouds. part I: Single-scattering and optical properties of hexagonal ice crystals, *J. Atmos. Sci.*, **46**, 3–18.
- Warren, S. G. (1984), Optical constants of ice from the ultraviolet to the microwave, *Appl. Opt.*, **23**, 1206–1225.
- Winker, D. M., J. Pelon, and M. P. McCormick (2003), The CALIPSO mission: Spaceborne lidar for observation of aerosols and clouds, *Proc. SPIE Int. Soc. Opt. Eng.*, **4893**, 1–11.
- Yang, P., and K. N. Liou (1996), Geometries-optics-integral-equation method for light scattering by nonspherical ice crystals, *Appl. Opt.*, **35**, 6568–6584.
- Yang, P., et al. (2001), Sensitivity of cirrus bidirectional reflectance to vertical inhomogeneous of ice crystals habits and size distribution for two Moderate-Resolution Imaging Spectroradiometer (MODIS), *J. Geophys. Res.*, **106**, 17,267–17,291.

P. Lawson, SPEC Inc., 5401 Western Avenue, Suite B, Boulder, CO 80301, USA.

M. McGill, NASA Goddard Space Flight Center, Code 912, Greenbelt, MD 20771, USA.

V. Noel, NASA Langley Research Center, Mail Stop 435, Hampton, VA 23681-2199, USA. (v.r.noel@larc.nasa.gov)

D. M. Winker, NASA Langley Research Center, Mail Stop 475, Hampton, VA 23681, USA.